JACS JOURNAL OF THE AMERICAN CHEMICAL SOCIETY
pubs.acs.org/JACS
Article

Oxygen Isotopologues Resolved from Water Oxidation Electrocatalysis by Electron Paramagnetic Resonance Spectroscopy

Trisha T. Nguyen, Richard I. Sayler, Aaron H. Shoemaker, Jibo Zhang, Stefan Stoll, Jay R. Winkler, R. David Britt,* and Bryan M. Hunter*

Cite This: J. Am. Chem. Soc. 2024, 146, 15019−15026

ABSTRACT: Electrocatalytic water oxidation is a key transformation in many strategies designed to harness solar energy and store it as chemical fuels. Understanding the mechanism(s) of the best electrocatalysts for water oxidation has been a fundamental chemical challenge for decades. Here, we quantitate evolved dioxygen isotopologue composition via gas-phase EPR spectroscopy to elucidate the mechanisms of water oxidation on metal oxide electrocatalysts with high precision. Isotope fractionation is paired with computational and kinetic modeling, showing that this technique is sensitive enough to differentiate O−O bond-forming steps. Strong agreement between experiment and theory indicates that for the nickel-iron layered double hydroxide—one of the best earth-abundant electrocatalysts to be studied—water oxidation proceeds via a dioxo coupling mechanism to form a side-bound peroxide rather than a hydroxide attack to form an end-bound peroxide.

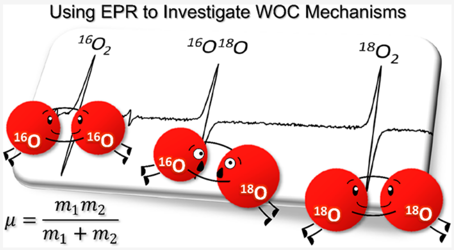

■ INTRODUCTION

The sun-driven electrochemical decomposition of water to oxygen and hydrogen gases, commonly known as solar water splitting, has been an increasingly popular topic for the advancement of noncarbon-based renewable fuels.[1] Nickel−iron oxides, $NiFeO_x$, are attractive water splitting catalysts because they efficiently facilitate the 4-electron oxidation of water (as evidenced by their low overpotentials), they are composed of earth-abundant metals, and they show excellent stability over time.[2] Nickel−iron layered double hydroxides ([NiFe]-LDHs) have recently come into focus as easily synthesizable by several methods and show particularly high current densities and Faradaic efficiencies.[3−5] Although [NiFe]-LDHs have been extensively studied, there remains significant uncertainty about the mechanism of water oxidation due to the complexity of the material and whether it operates differently than other catalysts, such as the archetypal iridium oxides. A hydroxide attack mechanism has been proposed, which involves the attack of water (or hydroxide) on a metal−oxo species to form an O−O bond.[6] We previously suggested that an intramolecular dioxo coupling may be an operative mechanism, and that water oxidation occurs at the high-valent oxidation state iron sites located at the 60° corner site.[3] The gold standard method for investigating these materials is to quantify the O_2 isotopologue products formed ($^{16}O_2$,^{16},$^{18}O_2$, $^{18}O_2$) when the ^{16}O-containing catalyst is introduced to, and oxidizes, $H_2{}^{18}O$. The use of membrane inlet mass spectrometry (MIMS)[7] and differential electrochemical mass spectrometry (DEMS)[8] marked a watershed in this field, which allowed for rapid time-course measurement of electrochemical properties *in situ*. The drawbacks are (1) the poor collection efficiency of oxygen, which radiates hemispherically from the electrode, and (2) the inability to quantify truly minute levels of oxygen. The latter is a major hurdle; oxygen produced at early times—even within the first turnover—is the most important quantity to measure since it has the potential to differentiate between the mechanisms currently proposed in the literature. Here, we introduce a complementary technique, gas-phase continuous-wave electron paramagnetic resonance (CW EPR) spectroscopy, to quantify the O_2 isotopologue products of several electrocatalysts for the oxygen evolution reaction (OER) in aqueous base. We demonstrate that this is a fast and ultrasensitive technique that provides insight into the mechanism of several important OER catalysts, compared to other spectroscopies, which measure bulk changes in oxidation state and fail to capture the kinetically "fast" states, which are critical to the mechanism.[3,9−11]

In situ spectroscopic methods have been recognized as critical to detect the reaction intermediates that may populate the catalytic cycle; while *ex situ* measurements are clarifying, their applicability to the real mechanism is at times uncertain.[12,13] *In situ* X-ray absorption spectroscopy (XAS) and Mössbauer spectroscopy have confirmed the existence of

Received: December 8, 2023
Revised: May 2, 2024
Accepted: May 3, 2024
Published: May 14, 2024

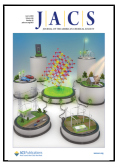

https://doi.org/10.1021/jacs.3c13868
J. Am. Chem. Soc. 2024, 146, 15019−15026

high-valent metal ions under working conditions.[9,11] Furthermore, surface Raman spectra identified both nickel−oxo and iron−oxo species, which may play different roles depending on the exact structure of the material (e.g., the concentration of nickel in an iron oxide matrix).[14] In summary, multiple active sites, such as $Ni^{3+/4+}$ and Fe^{4+}, and multiple intermediates, such as $M(=O)_2$ and M−O−O−M, have been identified.[13] These results have promoted a healthy debate within the community, and they demonstrate the need for further evidence to determine the atomic mechanism of the OER. However, the data are ambiguous and dependent on a multitude of experimental factors.

The emergence of various metal−oxygen species can be influenced by the applied potential because of capacitive behavior, and some may merely be spectators idle in the catalytic cycle.[3,5] Observation of a high concentration of an intermediate species may indicate that sequential OER steps are too sluggish to be "on path" for catalysis. Metal oxide catalysts also complicate water oxidation by allowing for both adsorbate evolution mechanisms (AEMs) and lattice oxygen-mediated mechanisms (LOMs).[15] AEMs suggest that O_2 evolution is mostly accomplished by redox transformations of water adsorbed onto the catalyst surface; this has been challenged by evidence, showing the incorporation of lattice oxygen in products.[16,17] To address this question, exquisite time resolution near the start of catalysis is necessary since the restructuring of lattice oxygen can be a competitive process.

Isotopic labeling can be used to probe the products of OER. Pioneering reports on ^{18}O labeling in water oxidation have revealed some participation of lattice oxygen in catalytic cycles,[15] and researchers have elucidated properties of the rate-limiting step through the study on kinetic isotope effects (KIEs) of $^{18}O/^{16}O$ reactivity.[16] Notably, Haschke et al. investigated the KIE by studying the ^{18}O enrichment after hours of steady-state electrolysis.[18] From these data, it was concluded that O−O bond formation is the rate-limiting step, corroborating other reports. Here, we propose that a methodology based on EPR spectroscopy and chronocoulometry would provide high sensitivity compared to existing methods.[8] EPR spectroscopy is capable of resolving and quantifying all O_2 isotopologues, and in conjunction, electrochemistry can quantify individual electrons via the integration of current (i).

■ RESULTS AND DISCUSSION

Resolution of Dioxygen Isotopologues by CW EPR.

Gas-phase O_2 in its spin-triplet ground state, with two unpaired electrons in its two π^* orbitals, features a unique X-band (~9.23 GHz) continuous-wave (CW) EPR spectrum, in which the combination of rotation, spin−spin coupling, spin−rotation coupling, and Zeeman interactions results in 100 observable transitions below 700 mT for $^{16}O_2$ at room temperature.[19,20] The sample must have enough O_2 to be detected, but not too much to cause broadening due to excess collisions, hence being EPR silent in atmosphere. Since rotational and spin−rotation coupling energies are dependent on the reduced mass, different O_2 isotopologues (including $^{16}O_2$, $^{16}O^{18}O$, and $^{18}O_2$) yield transitions at different magnetic fields.

Between 650 and 660 mT, each of these three oxygen isotopologues produces a strong EPR transition (Figure 1) corresponding to $(N, J, M_i \rightarrow M_f) = (1, 2, 0 \rightarrow 1)$ for $^{16}O_2$ and $^{18}O_2$ and $(N, J, M_i \rightarrow M_f) = (1, 2, -1 \rightarrow 1)$ for $^{16}O^{18}O$ (see Supporting Information for details)[19] and can be detected down to 0.547 nanomole of oxygen (Supplementary Figure 3). Possible gaseous contaminants are EPR silent. We use the double integrals of these three lines, in combination with calibration curves obtained from O_2 gas standard samples at various pressures, to determine the relative abundance of the isotopologues in the sample (Supplementary Figure 7). This approach was inspired by and previously used to study the bimolecular reaction of peroxyl radicals[21] and the thermal decomposition of $KBrO_3$.[22]

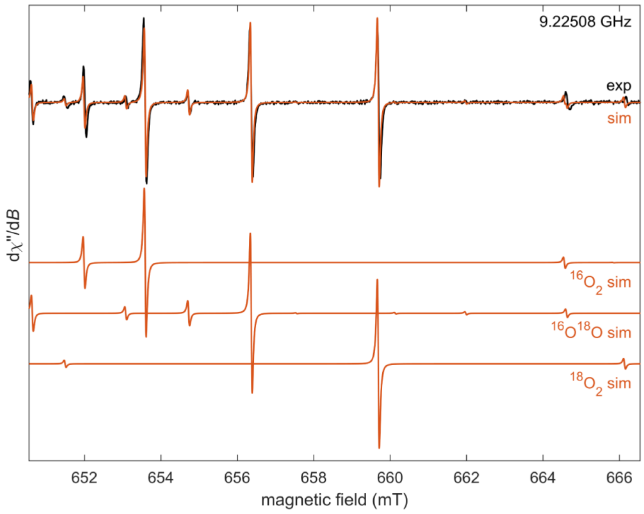

Figure 1. (Top) Experimental (black) and simulated (red) CW EPR spectrum of O_2 gas (21.73% $^{16}O_2$, 49.41% $^{16}O^{18}O$, 28.08% $^{18}O_2$, and 0.78% ^{17}O isotopologues). (Bottom) Individual simulated isotopologue spectra. Experimental parameters: 199 mTorr, room temperature, 2 mW microwave power, and 0.08 mT modulation amplitude. Simulations are based on parameters listed in Supplementary Table 1.

Here, we leverage the unique sensitivity of EPR detection of O_2 to study the initial turnover of oxygen on cobalt oxide (CoOx) and [NiFe]-LDH as well as the steady-state oxygen evolution on iridium oxide and [NiFe]-LDH.

Initial Oxygen Turnover on Cobalt Oxide and [NiFe]-LDH. We measured the CW EPR spectrum of the oxygen produced by ^{16}O-containing [NiFe]-LDH and CoO_x as a function of electrolysis time in 99 atom % ^{18}O-enriched water with 1 M KOH (hydroxide introduced by reacting labeled water with potassium metal to limit the amount of ^{16}O and Fe impurities introduced into the system). We then examined the spectra as a function of charge passed, which we converted to bulk turnover number based on the iron or cobalt loading (Figure 2). For experiments under constant anodic bias, we assumed that the lattice oxygen does not migrate to a significant degree, which has been previously reported in iron-containing systems,[23] and that the dioxygen isotopologues are indeed from the catalyst and not from the solvent.

Under these conditions, detection above 20 micromoles of oxygen is limited by collisional broadening of the EPR lines, and we observed key differences between the oxygen produced by cobalt oxide and [NiFe]-LDH. First, ^{18}O is incorporated within the first 0.1 turnover of cobalt oxide, detected as $^{18}O^{18}O$ (orange trace). Incorporation of ^{18}O does not appear until 0.2 turnovers for the layered double hydroxide, and even then, its incorporation is slow. After a full turnover, the ^{16}O content only falls to 94% for the LDH, compared to 50% within the first 0.1 turnover for cobalt oxide. From these data, we find

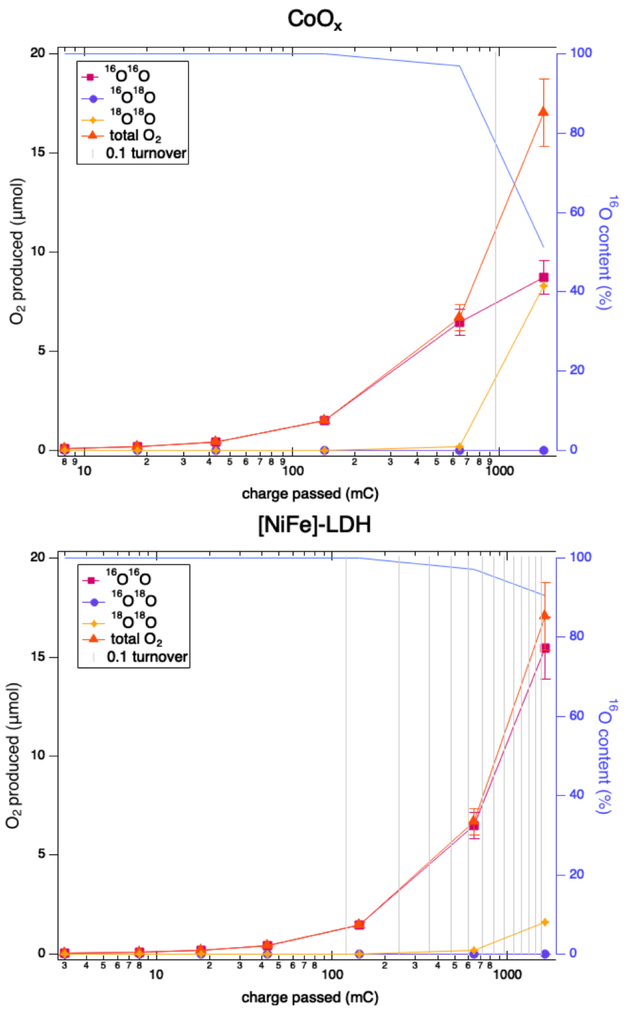

Figure 2. Dioxygen evolution from CoO$_x$ (top) and from [NiFe]-LDH (bottom) as a function of charge passed during electrolysis in 99% ^{18}O-enriched 1 M KOH. The abscissa indicates the charge passed. The left ordinate indicates the amount of oxygen produced of each isotopologue, down to submicromolar quantities. The right ordinate and the solid blue line indicate the fraction of ^{16}O in the dioxygen product calculated from the EPR spectra. Vertical gray lines each indicate 0.1 turnover, calculated from the number of active sites for both catalysts. Error bars are 10% of the integrated values.

agreement with the literature that there is little exchange between lattice hydroxide and solution hydroxide when the LDH catalysts are under potential; significant exchange would rapidly introduce ^{18}O within the first turnover. Second, no ^{16}O^{18}O is observed within the first turnover of the LDH, with a very small amount appearing after 0.1 turnover for CoO$_x$. The lower limit of reliable detection is approximately 0.547 nanomole (Supplementary Figure 3). We normalized turnovers to the iron and cobalt contents of the LDH and cobalt oxide, respectively (the Fe:Ni ratio is 1:3 in the LDH).

From these observations, we conclude that the mechanism of electrocatalytic water oxidation is different on cobalt oxides than it is on [NiFe]-LDH. Specifically, the [NiFe]-LDH fractionation is consistent with intramolecular coupling (Figure 3c), in that the initial isotopologues must come from the catalyst itself, followed by replacement of two sites by ^{18}O hydroxide. The isotopic fractionation for cobalt oxide is more complex since one would expect a significant amount of ^{16}O^{18}O via a water/hydroxide attack mechanism (Figure 3b). Although a small amount of ^{16}O^{18}O is detected after 0.1 turnover (3.3 nanomoles), ^{18}O^{18}O still predominates. This may arise from a smaller group of "fast" sites, which fully exchange early in the process, or it may be the result of kinetic and equilibrium isotope effects, which favor ^{18}O−^{18}O bond formation. The former may indicate that rapidly exchanging oxyl species are operative for cobalt oxide (Figure 3a).

Kinetic Isotope Analysis from Steady-State Concentrations on Iridium Dioxide and [NiFe]-LDH. To elucidate the mechanism of [NiFe]-LDH further, we measured the stepwise (pulsed applied potential) evolution of isotopologues for iridium oxide-catalyzed OER and compared it to that for the [NiFe]-LDH. Iridium oxide was chosen because computations overwhelmingly predict a hydroxide attack mechanism. These experiments are extremely sensitive and allowed us to measure the composition of O$_2$ produced at the subturnover level. This is virtually impossible to do with mass spectrometry since the collection efficiency of the generated dioxygen is lower and mass spectrometry is inaccurate when measuring trace amounts of ^{16}O$_2$. Some degree of oxygen mobility in the lattice is expected under these conditions since the catalyst does not remain under anodic bias.

For [NiFe]-LDH, what would have been the first turnover is observed to be partially a charging event, charging the nickel-based electrode from a Ni^{2+} state to a Ni^{3+} oxyhydroxide. Therefore, during this first "turnover," less oxygen is produced as the catalyst reaches its resting state. Iridium oxide, on the other hand, begins oxygen production more rapidly (Supplementary Figures 8 and 9). We assumed that the lattice oxygen does not migrate to a significant degree, which has been previously reported in iron-containing systems,[23] and our experiments showed little to no exchange in the resting state.

We considered two limiting mechanisms for O$_2$ evolution: hydroxide attack on a metal−oxo moiety ([MO]), and oxo coupling of two metal−oxo ([MOMO]) species (Figure 3b,a, respectively). We assumed that O−O bond formation was rate limiting, and that all other steps in the process are sufficiently rapid, so that concentrations can be described by equilibrium values. Given an isotopic composition of the alkaline media $\alpha \equiv [\mathrm{H}^{18}\mathrm{O}^-]/[\mathrm{H}^{16}\mathrm{O}^-]$, in the absence of isotopic equilibrium or kinetic fractionation, the relative isotopic compositions of the three isotopologues are expected to be

$$\frac{[{}^{16}\mathrm{O}_2]}{[{}^{16}\mathrm{O}_2]+[{}^{16}\mathrm{O}\,{}^{18}\mathrm{O}]+[{}^{18}\mathrm{O}_2]}=\frac{1}{(1+\alpha)^2} \quad (1a)$$

$$\frac{[{}^{16}\mathrm{O}\,{}^{18}\mathrm{O}]}{[{}^{16}\mathrm{O}_2]+[{}^{16}\mathrm{O}\,{}^{18}\mathrm{O}]+[{}^{18}\mathrm{O}_2]}=\frac{2\alpha}{(1+\alpha)^2} \quad (1b)$$

$$\frac{[{}^{18}\mathrm{O}_2]}{[{}^{16}\mathrm{O}_2]+[{}^{16}\mathrm{O}\,{}^{18}\mathrm{O}]+[{}^{18}\mathrm{O}_2]}=\frac{\alpha^2}{(1+\alpha)^2} \quad (1c)$$

In the hydroxide attack model (Figure 3b), the MO species is assumed to be at a steady-state concentration, and the predicted ratios of heavy to light O$_2$ are given by

$$\frac{[{}^{16}\mathrm{O}\,{}^{18}\mathrm{O}]}{[{}^{16}\mathrm{O}_2]}=\left(\frac{k_{{}^{18}\mathrm{OH}}}{k_{{}^{16}\mathrm{OH}}}+K_{\mathrm{M}^{18}\mathrm{O}/\mathrm{M}^{16}\mathrm{O}}\frac{k'_{{}^{16}\mathrm{OH}}}{k_{{}^{16}\mathrm{OH}}}\right)\alpha \quad (2a)$$

$$\frac{[{}^{18}\mathrm{O}_2]}{[{}^{16}\mathrm{O}_2]}=K_{\mathrm{M}^{18}\mathrm{O}/\mathrm{M}^{16}\mathrm{O}}\frac{k'_{{}^{18}\mathrm{OH}}}{k_{{}^{16}\mathrm{OH}}}\alpha^2 \quad (2b)$$

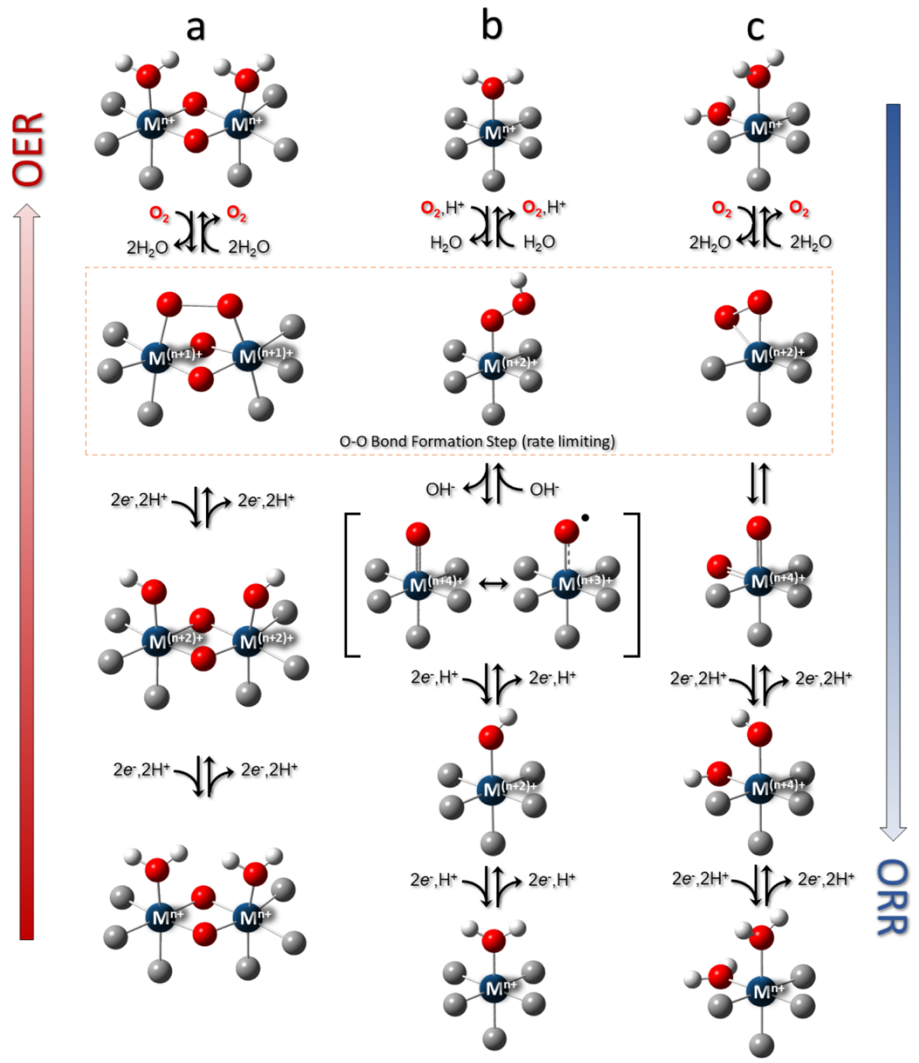

Figure 3. Three commonly proposed mechanisms for the OER. (a) Two-site M═O + M═O coupling, generally formulated as an oxyl radical attack. Both O atoms originate from the catalyst. (b) Water/hydroxide attacks on a nucleophilic metal oxo. The O–O bond is formed between unbound water/hydroxide and a metal–oxo or metal–oxyl species. (c) Intramolecular dioxo coupling on a single site. Both O atoms come from edge/lattice sites.

In eq 2a, the rate constants correspond to $H^{16}O^-$ attack on $M^{16}O$ ($k_{^{16}OH}$); $H^{16}O^-$ on $M^{18}O$ ($k'_{^{16}OH}$); $H^{18}O^-$ on $M^{16}O$ ($k_{^{18}OH}$); and $H^{18}O^-$ on $M^{18}O$ ($k'_{^{18}OH}$). The equilibrium constant $K_{M^{18}O/M^{16}O}$ corresponds to the following isotopic exchange reaction:

$$M^{16}O + H^{18}O^- \rightleftharpoons M^{18}O + H^{16}O^- \tag{3}$$

The ratios of rate constants appearing in eq 2a are expected to be <1 (normal mass-dependent kinetic isotope effects), whereas $K_{M^{18}O/M^{16}O}$ is expected to be ∼1.[24] Unless this equilibrium isotope fractionation is very large, the kinetic contributions are expected to dominate, leading to $[^{16}O^{18}O]$ and $[^{18}O_2]$ concentrations lower than expected based on α alone.

The oxo–oxo coupling model (Figure 3a) involves more equilibrium steps prior to the rate-limiting O–O bond formation. The predicted ratios of heavy to light O_2 are given by

$$\frac{^{16}O\,^{18}O}{^{16}O_2} = K_{(M^{16}O)(M^{18}O)/(M^{16}O)(M^{16}O)}\frac{k_{^{16}O\,^{18}O}}{k_{^{16}O\,^{16}O}}2\alpha \tag{4a}$$

$$\frac{^{18}O_2}{^{16}O_2} = K_{(M^{18}O)(M^{18}O)/(M^{16}O)(M^{16}O)}\frac{k_{^{18}O\,^{18}O}}{k_{^{16}O\,^{16}O}}\alpha^2 \tag{4b}$$

In eq 4a, the rate constants correspond to $k_{^{16}O\,^{16}O}$ to O–O coupling in $(M^{16}O)(M^{16}O)$; $k_{^{16}O\,^{18}O}k_{^{16}O\,^{18}O}$ to O–O coupling in $(M^{16}O)(M^{18}O)$; and $k_{^{18}O\,^{18}O}$ to O–O coupling in $(M^{18}O)(M^{18}O)$. The equilibrium constant $K_{(M^{16}O)(M^{18}O)/(M^{16}O)(M^{16}O)}$ corresponds to the following isotopic exchange reaction:

$$(M^{16}O)(M^{16}O) + H^{18}O^- \rightleftharpoons (M^{16}O)(M^{18}O) + H^{16}O^- \tag{5}$$

and the equilibrium constant $K_{(M^{18}O)(M^{18}O)/(M^{16}O)(M^{16}O)}$ corresponds to the following isotopic exchange reaction:

$$(M^{16}O)(M^{16}O) + 2H^{18}O^- \rightleftharpoons (M^{18}O)(M^{18}O) + 2H^{16}O^- \tag{6}$$

https://doi.org/10.1021/jacs.3c13868
J. Am. Chem. Soc. 2024, 146, 15019−15026

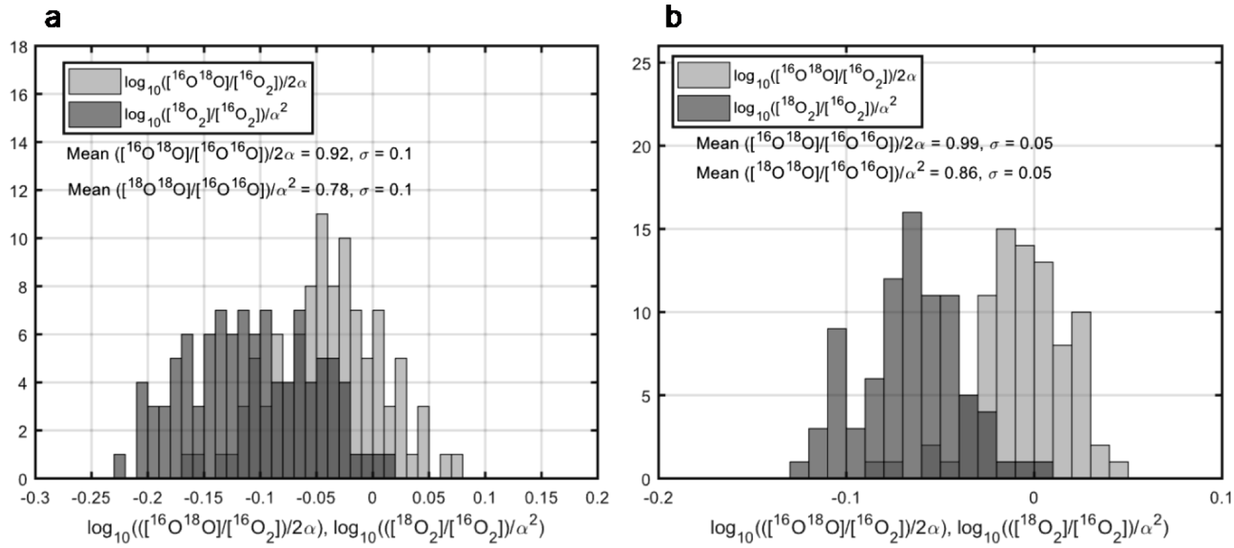

Figure 4. Histograms of ^{18}O enrichment factors for O_2 production using (a) [NiFe]-LDH and (b) IrO_2 electrocatalysts.

Table 1. Experimental and Calculated Isotopic Enrichment Factors for Dioxo Coupling and Hydroxide Attack on Iron and Iridium d^2 Models and a NiFe Dimer

		experimental		calculated		
species	mechanism	$\frac{[^{16}O\,^{18}O]}{[^{16}O_2]2\alpha}$	$\frac{[^{18}O_2]}{[^{16}O_2]\alpha^2}$	$\frac{[^{16}O\,^{18}O]}{[^{16}O_2]2\alpha}$	$\frac{[^{18}O_2]}{[^{16}O_2]\alpha^2}$	% diff
Fe(VI)	dioxo coupling	0.92	0.78	0.85	0.73	8.12%/7.54%
	hydroxide attack			0.80	0.64	15.25%/22.37%
Ni(III)−Fe(VI) dimer	dioxo coupling			0.84	0.72	8.88%/8.99%
Ir(VII)	dioxo coupling	0.99	0.86	1.03	0.98	4.24%/11.99%
	hydroxide attack			0.97	0.86	1.86%/0.11%

In this model, we anticipate that the ratios of rate constants will be <1, and the equilibrium constants will be ∼1. Additional derivation of the ideal isotopologue fractionations can be found in the SI (Supporting Information Section S6).

The time-dependent isotopic fractionation of OER on [NiFe]-LDH and IrO_2 electrodes was measured by EPR and related to the predicted statistical ratios (based on the isotopic enrichment for each run, α). The isotopic enrichment was calculated from the ^{18}O content of labeled water (typically ∼50%) and the added $K^{16}OH$. Histograms of the ratios of heavy to light O_2 divided by the predicted statistical ratios for OER on [NiFe]-LDH ($N = 35$) and IrO_2 ($N = 30$) are shown in Figure 4, and the experimental values for these ratios are summarized in Table 1. In general, the deviation from statistical ratios was greater for the [NiFe]-LDH catalyst than for IrO_2, though not different enough to make a mechanistic determination without the assistance of computational methods for the kinetic and equilibrium isotope effects defined above.

Computational Modeling. In an effort to contextualize the observed isotopic fractionation in Figure 4, we performed density functional theory (DFT) calculations on four model systems: the [NiFe]-LDH catalytic iron sites with high-valent iron(VI) dioxo and mono-oxo species and the IrO_2 with high-valent iridium(VII) dioxo and mono-oxo species. A common d^2 electron configuration was chosen as the basis for comparison, and detailed energies from these calculations are listed in the SI (Supporting Information Supplementary Table 2). In all cases, the singlet ($S = 0$) states were found to be higher in energy than the triplet ($S = 1$) states by 5−10 kcal/mol for Ir(VII) and over 20 kcal/mol for Fe(VI), making the singlet states inaccessible at room temperature. Lower valent Fe(IV) and Ir(V) mono-oxo species were computationally screened; however, we were unable to isolate reasonable transition states (i.e., transition states along the reaction coordinate) for the hydroxide attack model in these systems. Additionally, the pK_a of the calculated Ir(VI) mono-oxo species was too low to sustain adjacent explicit water molecules without deprotonation of an aqua ligand. For the dioxo coupling mechanism, we note that an Fe(IV) (d^4) metal has a π-system incapable of sustaining a dioxo moiety, confirming arguments that these sites would exist beyond the "oxo wall."[25] The corresponding Fe(II) peroxide species is likewise unreasonable. The hydroxide attack mechanisms were modeled using one explicit water molecule with both $[Fe(OH)_4(OH)(O)]^{3+}$ and $[Ir(OH)_4(OH)(O)]^{4+}$ species. Along the reaction coordinate, the water underwent deprotonation at the hydroxide ligand and subsequent attack at the metal-oxo site to form a protonated end-bound peroxide. It is important to note that the transition state for Ir(VII) involved a hydroxide attack mechanism, whereas that of Fe(VI) showed a water attack mechanism (e.g., no early deprotonation by the hydroxide ligand).

In the case of an oxo−oxo coupling mechanism, the reaction is predicted to be close to energetically neutral for a *cis*-dioxo Ir(VII) species (−2.85 kcal/mol) with a large activation energy

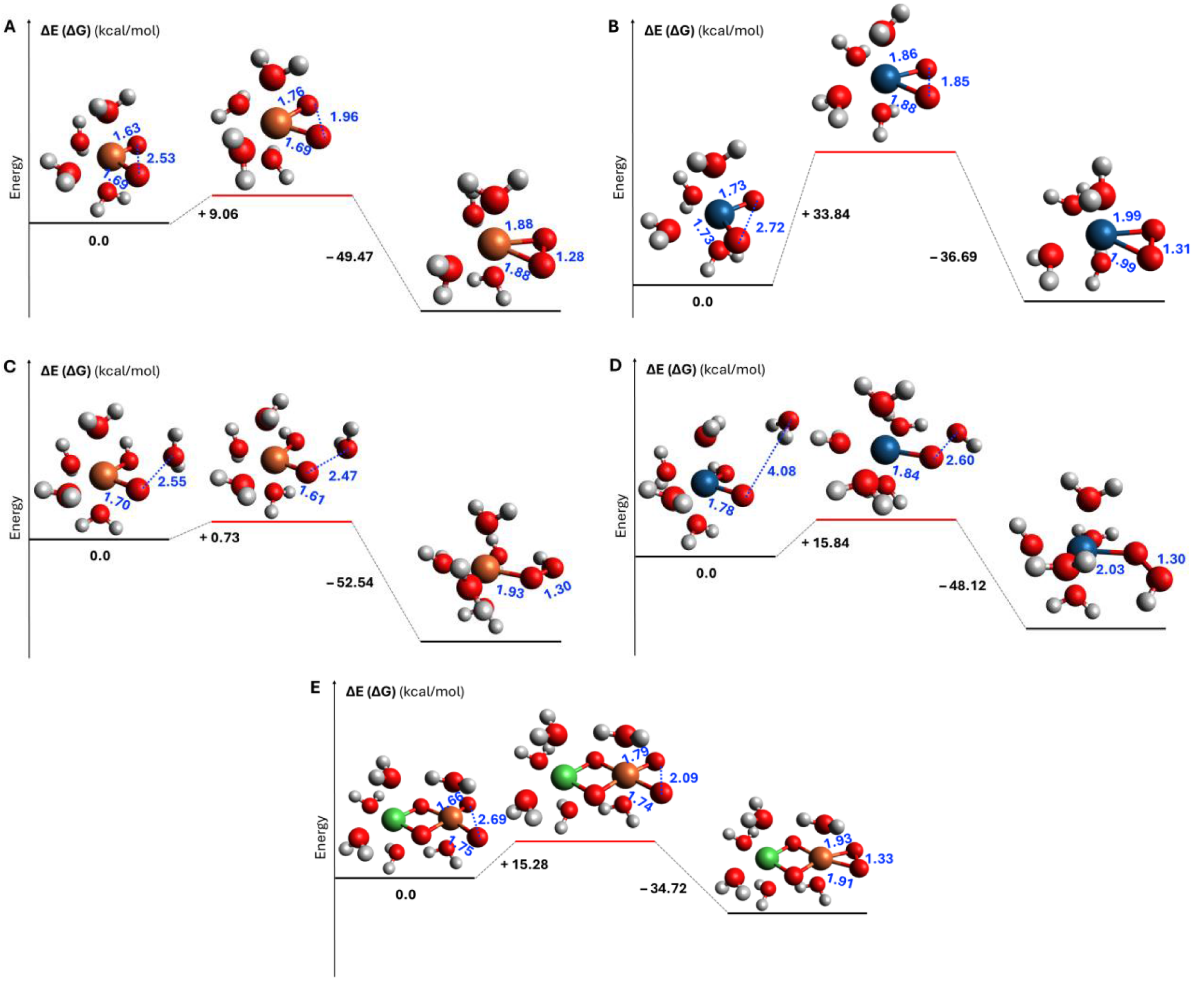

Figure 5. Energy diagrams from DFT calculations for model systems (a) Fe(VI) dioxo coupling, (b) Ir(VII) dioxo coupling, (c) Fe(VI) water attack, (d) Ir(VII) hydroxide attack, and (e) Ni(III)Fe(VI) dioxo coupling. M−O and O−O bond distances are in Angstroms, and changes in energies (Δ*G*) are in kcal/mol.

of 33.84 kcal/mol, but the reaction is relatively exothermic for the Fe(VI) case (−40.41 kcal/mol) with a small driving force of 9.06 kcal/mol to form the O−O bond. Furthermore, for the hydroxide attack mechanism at Ir(VII), the reaction has an activation energy of 15.84 kcal/mol and is exothermic by 32.28 kcal/mol, whereas water attack at Fe(VI) involves an activation energy of 0.73 kcal/mol and is exothermic by 51.81 kcal/mol. The energetics are depicted in Figure 5. Kinetic and equilibrium isotope effects were computed for each mechanism by searching for ground and transition states and augmenting the resulting Hessians with heavy oxygen (^{18}O). Nonelectronic contributions to the Gibbs free energy were compared to determine ratios of rate constants. Calculated rate constants were similar for both metals, indicating that the primary driver of the kinetic isotope effect is the metal-insensitive formation of the O−O bond. The calculated isotopic fractionation results are presented alongside experimental values in Table 1. A small scaling factor of 0.92 was applied to both the ratios of rate constants and in determining equilibrium isotope effects for dioxo coupling and hydroxide attack on iridium to bring the calculated values within range of the experimentally determined enrichment effects.

The calculated isotopic enrichment factors for oxo−oxo coupling at Fe(VI) showed close agreement with experimental values (8.12%/7.54% difference), whereby both enrichment factors were within one standard deviation of the mean for [NiFe]-LDH without the need for a scaling factor (the standard deviation for the IrO_2 experiments was 0.05, compared to 0.1 for [NiFe]-LDH). Worse agreement was shown for calculations simulating water attack at iron, in which the percent differences from experiment were 15.25%/22.37%—only within two standard deviations of the mean. From these models, we propose that dioxo coupling is the primary mechanism for O−O bond formation at Fe(VI), which is consistent with previous literature.[3,26] The calculated enrichment factors for hydroxide attack and dioxo coupling at Ir(VII), on the other hand, showed 1.86%/0.11% and 4.24%/11.99% deviation from the experimental values, respectively. Both enrichment factors calculated from the hydroxide attack simulations were well within one standard deviation of the experimental values. In the model for dioxo coupling, though the [$^{16}O^{18}O$]/[$^{16}O_2$] value was within one standard deviation from experiment, the value for [$^{18}O_2$]/[$^{16}O_2$] was beyond two standard deviations for a given α^2. Considering the thermodynamic data calculated for Ir(VII), it is predicted that dioxo coupling would be more rapid than hydroxide attack on IrO_2 ($\Delta\Delta G^{\ddagger} = -18$ kcal/mol), but hydroxide attack is a better model for the isotopic enrichment observed. Additionally, the mechanism of water oxidation occurring via water/hydroxide attack has already been precedented.[27,28] The dioxo coupling mechanism for a Ni(III)−Fe(VI) dimer was also computationally screened in order to determine any effect that a μ-oxo-bridged Ni(III) center would have on the kinetic isotope enrichment factors. However, the adjacent nickel site had no significant effect on either enrichment factor, showing 8.88%/8.99% difference from experiment—remarkably similar to the Fe(VI) case.

CONCLUSION

Compared to mass spectrometry that is unable to distinguish between atmospheric $^{16}O_2$ and $^{16}O_2$ evolved from water oxidation, X-band EPR spectroscopy has increased sensitivity due to resonance effects and, when paired with improved collection of oxygen gas, allows for the detailed analysis of isotopologues from cobalt oxide, iridium oxide, and nickel−iron layered double hydroxides. A study of the initial composition of O_2 evolved implicates that [NiFe]-LDH incorporates significantly more lattice oxygen than cobalt oxide. Computational modeling using DFT found the isotopic enrichment factors (eqs4a and 4b) to be robust and resistant to computational fluctuations due to their interrelated parameters, e.g., KIEs and equilibrium constants that appear in both ratios and energies, which form the basis of multiple rate constants. We conclude that O−O bond formation for nickel−iron layered double hydroxide electrocatalysts likely occurs by dioxo coupling, modeled here on the same high-valent iron center. Water oxidation on iridium oxide, however, is better described as a hydroxide attack, though we cannot rule out that both mechanisms may proceed simultaneously based on the computations reported herein. This technique is broadly applicable to the large class of water oxidation electrocatalysts and can be used to differentiate mechanisms by examining the initial steps of the oxygen evolution reaction. By discriminating between O−O bond-forming steps that have been debated for decades, we envision efforts to design better catalytic materials and bring this technology closer to feasibility.

ASSOCIATED CONTENT

Supporting Information

The Supporting Information is available free of charge at https://pubs.acs.org/doi/10.1021/jacs.3c13868.

Experimental methods, EPR spectroscopy, kinetic modeling, DFT calculations; experimental CW EPR spectrum of $^{16}O_2$ at room temperature and 9.529533 GHz (Supplementary Figure 1); extended range experimental CW EPR spectrum of $^{16}O_2$ at room temperature (Supplementary Figure 2); experimental CW EPR spectrum of $^{16}O_2$ at room temperature at 0.547 nmol of $^{16}O_2$ (Supplementary Figure 3); schematic for the custom manifold designed for the O_2 experiment (Supplementary Figure 4); day 0 calibration curve samples, measured before the samples were flame sealed (Supplementary Figure 5); EPR spectrum and absorption spectrum of the 396 mTorr calibration sample containing 21.73% $^{16}O_2$, 49.41% $^{16}O^{18}O$, 28.08% $^{18}O_2$, and 0.78% other ^{17}O isotopologues, measured before the sample was flame sealed (Supplementary Figure 6); calibration curve data correlating peak area to relative amount in sample in nmol for $^{16}O^{16}O$, $^{16}O^{18}O$, and $^{18}O^{18}O$ (Supplementary Figure S7); electrolysis data for 2.0 mg of [NiFe]-LDH (Supplementary Figure 8); electrolysis data for 0.6 mg of IrO_2 (Supplementary Figure 9); [NiFe]-LDH electrolysis data (Supplementary Figure 10); IrO_2 electrolysis data (Supplementary Figure 11); [NiFe]-LDH enrichment data (Supplementary Figure 12); and IrO_2 enrichment data (Supplementary Figure 13); Hamiltonian parameters used in the simulation of O_2 EPR spectra (Supplementary Table 1); calculated final Gibbs free energies for all relevant species (Supplementary Table 2); thermochemistry ^{18}O augmentation data (Supplementary Tables 3−12); Cartesian coordinates (*xyz*) and energies (Supplementary Table 13) (PDF)

AUTHOR INFORMATION

Corresponding Authors

R. David Britt − *Department of Chemistry, University of California, Davis, Davis, California 95616, United States;* orcid.org/0000-0003-0889-8436; Email: rdbritt@ucdavis.edu

Bryan M. Hunter − *Department of Chemistry, University of California, Davis, Davis, California 95616, United States; Department of Chemistry, Northwestern University, Evanston, Illinois 60208, United States; Rowland Institute at Harvard, Harvard University, Cambridge, Massachusetts 02138, United States;* orcid.org/0000-0001-8559-9304; Email: bhunter@northwestern.edu

Authors

Trisha T. Nguyen − *Department of Chemistry, University of California, Davis, Davis, California 95616, United States*

Richard I. Sayler − *Department of Chemistry, University of California, Davis, Davis, California 95616, United States*

Aaron H. Shoemaker − *Department of Chemistry, Northwestern University, Evanston, Illinois 60208, United States*

Jibo Zhang − *Department of Chemistry, Northwestern University, Evanston, Illinois 60208, United States*

Stefan Stoll − *Department of Chemistry, University of Washington, Seattle, Washington 98195, United States*

Jay R. Winkler − *Division of Chemistry and Chemical Engineering, California Institute of Technology, Pasadena, California 91125, United States;* orcid.org/0000-0002-4453-9716

Complete contact information is available at: https://pubs.acs.org/10.1021/jacs.3c13868

Notes

The authors declare no competing financial interest.

ACKNOWLEDGMENTS

B.M.H. is grateful for a Fellowship from the Rowland Institute at Harvard. R.D.B. acknowledges support for operating the CalEPR facility at UC Davis by National Institutes of Health grant 1R35GM126961 and research support from the Winston Ko Chair in Science Leadership and the Miller Institute for Basic Research in Science, University of California, Berkeley. This research was supported in part through the computational resources and staff contributions provided for the Quest high performance computing facility at Northwestern University, which is jointly supported by the Office of the Provost, the Office for Research, and Northwestern University Information Technology.

■ REFERENCES

(1) Gray, H. B. Powering the Planet with Solar Fuel. *Nat. Chem.* **2009**, *1*, 7.

(2) Hunter, B. M.; Gray, H. B.; Müller, A. M. Earth-Abundant Heterogeneous Water Oxidation Catalysts. *Chem. Rev.* **2016**, *116*, 14120−14136.

(3) Hunter, B. M.; Thompson, N. B.; Müller, A. M.; Rossman, G. R.; Hill, M. G.; Winkler, J. R.; Gray, H. B. Trapping an Iron(VI) Water-Splitting Intermediate in Nonaqueous Media. *Joule* **2018**, *2*, 747−763.

(4) Gong, M.; Dai, H. A mini review of NiFe-based materials as highly active oxygen evolution reaction electrocatalysts. *Nano Res.* **2015**, *8*, 23−39.

(5) Görlin, M.; Chernev, P.; Ferreira de Araújo, J.; Reier, T.; Dresp, S.; Paul, B.; Krähnert, R.; Dau, H.; Strasser, P. Oxygen Evolution Reaction Dynamics, Faradaic Charge Efficiency, and the Active Metal Redox States of Ni−Fe Oxide Water Splitting Electrocatalysts. *J. Am. Chem. Soc.* **2016**, *138*, 5603−5614.

(6) He, Z.; Zhang, J.; Gong, Z.; Lei, H.; Zhou, D.; Zhang, N.; Mai, W.; Zhao, S.; Chen, Y. Activating lattice oxygen in NiFe-based (oxy)hydroxide for water electrolysis. *Nat. Commun.* **2022**, *13*, 2191.

(7) Poulsen, A. K.; Rompel, A.; Mckenzie, C. J. Water Oxidation Catalyzed by a Dinuclear Mn Complex: A Functional Model for the Oxygen-Evolving Center of Photosystem II. *Angew. Chem., Int. Ed.* **2005**, *44*, 6916−6920.

(8) Ullman, A. M.; Brodsky, C. N.; Li, N.; Zheng, S. L.; Nocera, D. G. Probing Edge Site Reactivity of Oxidic Cobalt Water Oxidation Catalysts. *J. Am. Chem. Soc.* **2016**, *138*, 4229−4236.

(9) Friebel, D.; Louie, M. W.; Bajdich, M.; Sanwald, K. E.; Cai, Y.; Wise, A. M.; Cheng, M.-J.; Sokaras, D.; Weng, T.-C.; Alonso-Mori, R.; et al. Identification of Highly Active Fe Sites in (Ni,Fe)OOH for Electrocatalytic Water Splitting. *J. Am. Chem. Soc.* **2015**, *137*, 1305−1313.

(10) Li, N.; Hadt, R. G.; Hayes, D.; Chen, L. X.; Nocera, D. G. Detection of high-valent iron species in alloyed oxidic cobaltates for catalysing the oxygen evolution reaction. *Nat. Commun.* **2021**, *12*, 4218.

(11) Chen, J. Y. C.; Dang, L.; Liang, H.; Bi, W.; Gerken, J. B.; Jin, S.; Alp, E. E.; Stahl, S. S. Operando Analysis of NiFe and Fe Oxyhydroxide Electrocatalysts for Water Oxidation: Detection of Fe^{4+} by Mössbauer Spectroscopy. *J. Am. Chem. Soc.* **2015**, *137*, 15090−15093.

(12) Fabbri, E.; Abbott, D. F.; Nachtegaal, M.; Schmidt, T. J. Operando X-ray absorption spectroscopy: A powerful tool toward water splitting catalyst development. *Curr. Opin. Electrochem.* **2017**, *5*, 20−26.

(13) Chen, S.; Ma, L.; Huang, Z.; Liang, G.; Zhi, C. In situ/operando analysis of surface reconstruction of transition metal-based oxygen evolution electrocatalysts. *Cell Rep. Phys. Sci.* **2022**, 3, 100729.

(14) Bai, L.; Lee, S.; Hu, X. Spectroscopic and Electrokinetic Evidence for a Bifunctional Mechanism of the Oxygen Evolution Reaction. *Angew. Chem., Int. Ed.* **2021**, *60*, 3095−3103.

(15) Grimaud, A.; Diaz-Morales, O.; Han, B.; Hong, W. T.; Lee, Y.-L.; Giordano, L.; Stoerzinger, K. A.; Koper, M. T. M.; Shao-Horn, Y. Activating lattice oxygen redox reactions in metal oxides to catalyse oxygen evolution. *Nat. Chem.* **2017**, *9*, 457−465.

(16) Li, C.; Ju, W.; Vijay, S.; Timoshenko, J.; Mou, K.; Cullen, D. A.; Yang, J.; Wang, X.; Pachfule, P.; Brückner, S.; et al. Covalent Organic Framework (COF) Derived Ni-N-C Catalysts for Electrochemical CO_2 Reduction: Unraveling Fundamental Kinetic and Structural Parameters of the Active Sites. *Angew. Chem., Int. Ed.* **2022**, *61*, No. e202114707.

(17) Trześniewski, B. J.; Diaz-Morales, O.; Vermaas, D. A.; Longo, A.; Bras, W.; Koper, M. T. M.; Smith, W. A. In Situ Observation of Active Oxygen Species in Fe-Containing Ni-Based Oxygen Evolution Catalysts: The Effect of pH on Electrochemical Activity. *J. Am. Chem. Soc.* **2015**, *137*, 15112−15121.

(18) Haschke, S.; Mader, M.; Schlicht, S.; Roberts, A. M.; Angeles-Boz, A. M.; Barth, J. A. C.; Bachmann, J. Direct oxygen isotope effect identifies the rate-determining step of electrocatalytic OER at an oxidic surface. *Nat. Commun.* **2018**, *9* (1), 4565.

(19) Tinkham, M.; Strandberg, M. W. P. Interaction of Molecular Oxygen with a Magnetic Field. *Phys. Rev.* **1955**, *97*, 951−966.

(20) Tinkham, M.; Strandberg, M. W. P. Theory of the Fine Structure of the Molecular Oxygen Ground State. *Phys. Rev.* **1955**, *97*, 937−951.

(21) Bennett, J. E.; Howard, J. A. Bimolecular Self-Reaction of Peroxy Radicals. An Oxygen-18 Isotope Study. *J. Am. Chem. Soc.* **1973**, *95*, 4008−4010.

(22) Bjerre, N.; Larsen, E. Determination of the isotopic composition of oxygen by electron spin resonance spectrometry. *Anal. Chem.* **1983**, *55*, 2236−2238.

(23) Lee, S.; Banjac, K.; Lingenfelder, M.; Hu, X. Oxygen Isotope Labeling Experiments Reveal Different Reaction Sites for the Oxygen Evolution Reaction on Nickel and Nickel Iron Oxides. *Angew. Chem.* **2019**, *131*, 10401−10405.

(24) Anbar, M.; Taube, H. Oxygen Isotope Effects at Anodes. *J. Am. Chem. Soc.* **1956**, *78*, 3252−3255.

(25) Gray, H. B.; Winkler, J. R. Living with Oxygen. *Acc. Chem. Res.* **2018**, *51*, 1850−1857.

(26) Kurtz, D. A.; Hunter, B. M. Forming O-O bonds. *Joule* **2022**, *6*, 2272−2292.

(27) Blakemore, J. D.; Schley, N. D.; Balcells, D.; Hull, J. F.; Olack, G. W.; Incarvito, C. D.; Eisenstein, O.; Brudvig, G. W.; Crabtree, R. H. Half-Sandwich Iridium Complexes for Homogeneous Water-Oxidation Catalysis. *J. Am. Chem. Soc.* **2010**, *132*, 16017−16029.

(28) González, D.; Sodupe, M.; Rodríguez-Santiago, L.; Solans-Monfort, X. Metal coordination determines the catalytic activity of IrO_2 nanoparticles for the oxygen evolution reaction. *J. Catal.* **2022**, *412*, 78−86.